remote sensing

MDPI

Article

Improving the Spatiotemporal Resolution of Land Surface Temperature Using a Data Fusion Method in Haihe Basin, China

Rencai Lin, Zheng Wei *, He Chen, Congying Han, Baozhong Zhang and Maomao Jule

State Key Laboratory of Simulation and Regulation of Water Cycle in River Basin, China Institute of Water Resources and Hydropower Research, Beijing 100048, China; rencaihrs@iwhr.com (R.L.); chenhe@iwhr.com (H.C.); hancy@iwhr.com (C.H.); zhangbz@iwhr.com (B.Z.); julemaomao@edu.iwhr.com (M.J.)
* Correspondence: weizheng@iwhr.com; Tel.: +86-187-1004-7605

Abstract: Land surface temperature (LST) serves as a pivotal component within the surface energy cycle, offering fundamental insights for the investigation of agricultural water environment, urban thermal environment, and land planning. However, LST monitoring at a point scale entails substantial costs and poses implementation challenges. Moreover, the existing LST products are constrained by their low spatiotemporal resolution, limiting their broader applicability. The fusion of multi-source remote sensing data offers a viable solution to enhance spatiotemporal resolution. In this study, the Enhanced Spatial and Temporal Adaptive Reflectance Fusion Model (ESTARFM) was used to estimate time series LST utilizing multi-temporal Landsat 8 (L8) and MOD21A2 within the Haihe basin in 2021. Validation of ESTARFM LST was conducted against L8 LST and in situ LST. The results can be summarized as follows: (1) ESTARFM was found to be effective in heterogeneous regions within the Haihe basin, yielding LST with a spatiotemporal resolution of 30 m and 8 d while retaining clear texture information; (2) the comparison between ESTARFM LST and L8 LST shows a coefficient determination (R^2) exceeding 0.59, a mean absolute error (MAE) lower than 2.43 K, and a root mean square error (RMSE) lower than 2.63 K for most dates; (3) comparison between ESTARFM LST and in situ LST showcased high validation accuracy, revealing a R^2 of 0.87, a MAE of 2.27 K, and a RMSE of 4.12 K. The estimated time series LST exhibited notable reliability and robustness. This study introduced ESTARFM for LST estimation, achieving satisfactory outcomes. The findings offer a valuable reference for other regions to generate LST data with a spatiotemporal resolution of 8 d and 30 m, thereby enhancing the application of data products in agriculture and hydrology contexts.

Keywords: land surface temperature; ESTARFM; Landsat 8; MOD21A2

check for updates

Citation: Lin, R.; Wei, Z.; Chen, H.; Han, C.; Zhang, B.; Jule, M. Improving the Spatiotemporal Resolution of Land Surface Temperature Using a Data Fusion Method in Haihe Basin, China. *Remote Sens.* **2024**, *16*, 2374. https://doi.org/10.3390/rs16132374

Academic Editor: Bo-Hui Tang

Received: 10 April 2024
Revised: 7 June 2024
Accepted: 26 June 2024
Published: 28 June 2024

Copyright: © 2024 by the authors. Licensee MDPI, Basel, Switzerland. This article is an open access article distributed under the terms and conditions of the Creative Commons Attribution (CC BY) license (https://creativecommons.org/licenses/by/4.0/).

1. Introduction

Land surface temperature (LST) serves as a crucial variable within climatic, ecological, and biogeochemical models, influencing diverse domains such as vegetation growth, climate dynamics, and human activities [1]. The realm of applications for LST is vast, spanning agroecosystem [2,3], urban thermal environment [4–6], crop evapotranspiration estimation [7–9], and surface soil moisture estimation [10–12].

The measurement of LST encompasses a range of methodologies, including field observation [13], inversion techniques relying on thermal infrared remote sensing imagery [14], and simulation through land surface models [15]. The field observation methods include both manual and automated observation techniques. While effective in capturing LST with high temporal resolution at specific points, these methods are inherently limited in their capacity to provide LST data on a regional scale. Furthermore, this approach demands substantial labor and financial resources, thus posing challenges to its widespread adoption and applicability. The method founded upon thermal infrared remote sensing images predominantly harnesses the thermal infrared band of optical remote sensing satellites, including Landsat 7/8 and FY-3, to retrieve LST. Notably, this method encompasses distinct

algorithms such as the single-channel algorithm [16], the split window algorithm [17], and the multi-channel algorithm [18]. In contrast, land surface process simulation involving physical processes and dynamic mechanisms stands as a primary avenue for obtaining comprehensive land surface information with elevated spatiotemporal resolution. This method excels at generating spatially complete, daily, or hourly continuous LST datasets. Additionally, Land Surface Models (LSMs) integrated into established land data assimilation systems, such as the China Land Data Assimilation System (CLDAS) [19], the North American Land Data Assimilation System (NLDAS) [20], and the Global Land Data Assimilation System (GLDAS) [21], offer prognostic capabilities for predicting spatially comprehensive and temporally continuous LST (e.g., on daily or hourly timescales). However, it is important to note the spatial resolution of these outputs is relatively coarse, e.g., approximately ~7 km × 7 km for LST output from CLDAS and ~14 km × 14 km for LST output from NLDAS. At the same time, it is pertinent to acknowledge the inherent complexities in simulating land surface processes. Challenges include accounting for the heterogeneity of land surfaces, the diversity of land cover types, and the intricacies associated with parameterization.

The remote sensing data used in LST retrieval are primarily within the thermal infrared spectrum. However, thermal infrared temperature retrieval algorithms are effective only under clear sky conditions and often suffer from disruptions caused by clouds and adverse weather phenomena [22]. This limitation results in incomplete land cover representation across many LST products. For instance, more than 60% of MODIS LST are impacted by clouds and other adverse conditions [23]. Attempts have been made to enhance the utility of MODIS LST data by developing the MOD11A2 with a temporal resolution of 8 d. Yet, these data remain discontinuous over time and have a coarse spatial resolution (1 km). In contrast, passive microwave remote sensing-based LST retrievals experience lesser susceptibility to adverse weather conditions, albeit at the cost of spatial resolution. The pursuit of dynamic resources and environmental monitoring necessitates LST information that is spatially comprehensive, relatively continuous in time, and boasts high spatial resolution. Regrettably, existing LST products fall short of meeting these application requirements. To overcome this shortfall, scholars have begun to explore techniques such as space–time interpolation [24] or data fusion methods to generate multi-source remote sensing LST datasets [13,25–27]. A plethora of data fusion methods, including the Spatial and Temporal Adaptive Reflectance Fusion Model (STARFM) [28], the Enhanced Spatial and Temporal Adaptive Reflectance Fusion Model (ESTARFM) [29], the Flexible Spatiotemporal Data Fusion (FSDAF) [30], and the Cubesat Enabled Spatiotemporal Enhancement Method (CESTEM) [31], have gained widespread adoption. Scholars have also explored the integration of additional data sources. Amazirh et al. [32] introduced Sentinel-1 images to enhance MODIS LST decomposition. Kou et al. [33] proposed a fusion method between MODIS LST and AMSR-E LST using Bayesian Maximum Entropy, yielding promising outcomes on the Tibetan Plateau, China, with fusion accuracy ranging from 2.31 K to 4.53 K. These fusion methods counteract the grid effect of LST through statistical interpolation, enabling a partial reflection of temperature variation details within the gap areas. Furthermore, Long et al. [34] and Abowarda et al. [35] used ESTARFM for spatial downscaling of MOD11A1 LST, leveraging it as a downscaling factor for soil moisture downscaling. Ultimately, this approach enabled the derivation of daily soil moisture with a spatial resolution of 1 km and 30 m at a regional scale. It is worth noting that scholars have achieved significant positive outcomes in their research on utilizing machine learning combined with data fusion for generating time series LST. Xu et al. [36] utilized the random forest to fuse Passive Microwave (PMW) LST and Thermal Infrared (TIR) LST, resulting in a fused LST dataset for the year 2010 in China. Weng et al. [37] made improvements to the existing Spatiotemporal Adaptive Reflectance Fusion Model (STARFM) by considering annual temperature cycles and urban thermal landscape heterogeneity. They applied this enhanced model to predict LST data, obtaining predictive results for LST over a 5 d period in Los Angeles County, CA, USA, spanning from July to October in 2005.

In conclusion, the practical utilization of existing LST products presents notable challenges when applied at a regional scale. Current algorithms are tailored to specific regions, yielding LST products characterized by limited spatiotemporal resolution. Even in cases of fused LST products, their applicability often remains confined to targeted regions. In the context of validation methods, many studies resort to artificial measurements of LST for validation, a technique that can yield high accuracy. However, this manual method is not only time-consuming but also labor-intensive. Given these circumstances, the search for an alternative validation method is imperative—one that obviates the need for manual monitoring while still ensuring a certain level of accuracy in the spatial distribution data of LST. In response, this study introduces a novel approach: real-time monitoring of meteorological data to calculate LST for validation. Remarkably, this alternative validation method also yields a heightened level of accuracy. Such innovation holds the potential to drive advancements within this field, facilitating its continued development.

The Haihe basin, situated in northern China, encompasses two major municipalities, Beijing and Tianjin, along with several other provinces. This basin meets the needs of around 10% of China's population and contributes about 8% of the nation's cultivated land. Its pivotal role extends to politics, economy, culture, and agriculture. Notably, corn and wheat cultivation thrive within this basin [38]. While various remote sensing technologies and data fusion methods, including ESTARFM, have shown significant promise in enhancing spatial and temporal resolution, several limitations and challenges remain, particularly in complex environments like the Haihe Basin. One of the primary limitations of ESTARFM is its dependency on high-quality input images from both the fine- and coarse-resolution sensors. In regions like the Haihe Basin, where atmospheric conditions frequently obscure satellite imagery, the availability of such high-quality images is often compromised [29]. Additionally, the heterogeneous landscape of the Haihe Basin, characterized by a mix of urban, agricultural, and natural land covers, poses significant challenges for accurate data fusion. The model's performance can degrade when dealing with abrupt changes in land cover or significant phenological variations, leading to inaccuracies in the predicted fine-resolution images [28]. Moreover, ESTARFM's computational complexity and the requirement for substantial processing power can be a limiting factor, especially when large datasets over extended periods need to be processed [39].

Previous studies have applied ESTARFM to conduct surface soil moisture downscaling studies in the Haihe basin and achieved good results [35]. This study wants to know how adaptive ESTARFM is to the fusion of LST in the Haihe Basin. So, the ESTARFM was used for estimating time series LST through the integration of multi-temporal L8 and MOD21A2. The efficacy and resilience of the fusion outcomes were assessed through validation against both L8 LST and in situ LST. The proposed method underwent testing within Area 1 and Area 2 of the Haihe basin, China, as depicted in Figure 1. This study primarily focuses on validating the efficacy of the ESTARFM for LST fusion within the Haihe basin. The goal is to establish a dependable method for obtaining LST with enhanced spatiotemporal resolution.

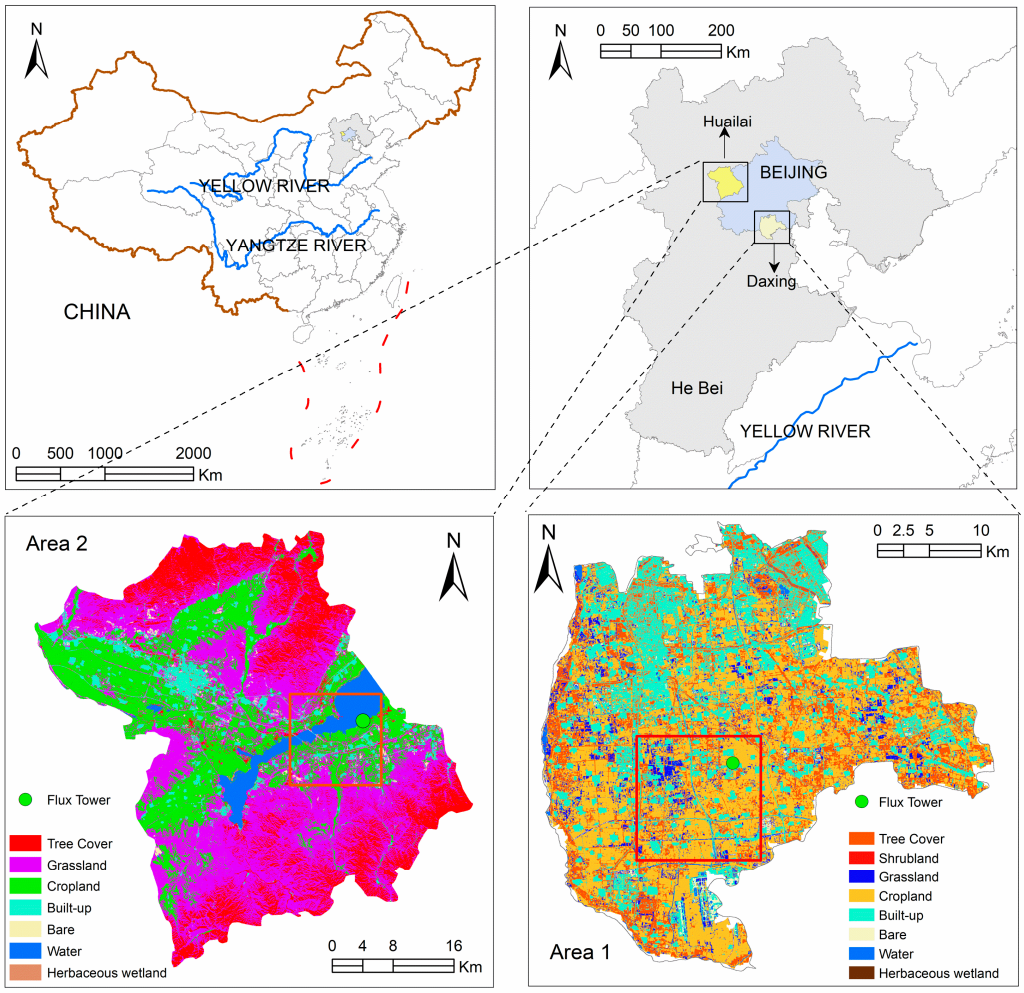


Figure 1. Geographical location of Area 1 and Area 2. The red frame is the range of the final result of this study, and its area is 12 km × 12 km.

2. Materials and Methods

2.1. Study Area

The Haihe basin (35°01′–42°45′N, 111°57′–119°51′E, Figure 1) is situated in northern China. It encompasses the two influential municipalities of Beijing and Tianjin, a significant portion of Hebei province, and stretches into parts of Shanxi, Shandong, Inner Mongolia, Liaoning, and Henan provinces. The topography of the basin features higher terrain in the northwest transitioning to lower regions in the southeast, with a prominent monsoon climate. The annual average air temperature (T_a) stands at approximately 10 °C, and the annual average precipitation records 539 mm. The precipitation distribution varies significantly, with 80% occurring from May to October. The annual average relative humidity falls within the range of 50% to 70%. Daxing District (Area 1) and Huailai County (Area 2) were selected as representative areas for validation and study. Daxing District situated to the south of Beijing, spans an area of 1036.33 km^2, measuring 43 km in length and 45 km in wide. It has a permanent population of 1.545 million [40]. Meanwhile, Huailai County located in the northwest of Hebei province and the southeast of Zhangjiakou, shares borders with Yanqing District, Changping District, and Mentougou District of Beijing. Covering an area of 1801 km^2, Huailai County hosts a population of approximately 367,000.

2.2. Data

This study incorporates a diverse range of data sources, encompassing remote sensing data and meteorological data. Each of these data categories serves a specific purpose within

the research framework. Remote sensing images are used for the retrieval and fusion of LST. In contrast, meteorological data finds utility in calculating LST, which subsequently acts as the reference LST for the validation of the time series LST at a spatial resolution of 30 m. This study chose 2021 as the research period mainly due to the quality of MOD21A2 and L8 data in 2021, which are the best in recent years. In the future, this method can be extended to other periods.

2.2.1. Landsat 8

Landsat 8 (L8) represents the eighth iteration of the Landsat satellite series, propelled into orbit by the National Aeronautics and Space Administration (NASA) on 11 February 2013. This satellite carries dual sensor capabilities: the Operational Land Imager (OLI) and the Thermal Infrared Sensor (TIRS). The OLI consists of 9 bands, with the panchromatic band processing a spatial resolution of 15 m, while other bands offer a spatial resolution of 30 m, collectively covering an imaging width of 185 km × 185 km. Meanwhile, the TIRS is equipped with two thermal infrared bands with a spatial resolution of 100 m. The specific band information is detailed in Table 1. The satellite is in a near-polar orbit or sun-synchronous orbit. For this research, L8 images have been made accessible to users through the United States Geological Survey (USGS) without any associated cost (http://glovis.usgs.gov/, accessed on 1 January 2023. The L8 satellite transited the study area at approximately 10:00 AM local time.

Table 1. Band information of Landsat-8 (L8).

Sensor	Band	Bandwidth/μm	Spatial Resolution/m
Operational Land Imager (OLI)	Coastal	0.43–0.45	30
	Blue	0.45–0.51	30
	Green	0.53–0.59	30
	Red	0.64–0.67	30
	NIR	0.85–0.88	30
	SWIR1	1.57–1.65	30
	SWIR2	2.11–2.29	30
	Pan	0.50–0.68	15
	Cirrus	10.6–11.19	30
Thermal Infrared Sensor (TIRS)	TIRS1	10.6–11.19	100
	TIRS2	11.5–12.51	100

2.2.2. MOD21A2

The MODIS data utilized for this study is MOD21A2, obtained from the sensor mounted on the Terra satellite. The MOD21A2 dataset is an 8-day composite LST product at 1000 m spatial resolution that uses an algorithm based on a simple averaging method. To access this product, interested parties can download it from the National Aeronautics and Space Administration (NASA) (https://ladsweb.modaps.eosdis.nasa.gov/search, accessed on 1 January 2023). Subsequently, the data underwent a reprojection process into the Universal Transverse Mercator (UTM) map projection system, a transformation accomplished using the Modis Conversion Toolkit (MCTK). Furthermore, the data were cropped along the perimeter of the designated study area. To ensure congruence with L8, the nearest neighbor algorithm was employed to resample the MOD21A2 to a spatial resolution of 30 m, matching the row and column dimensions of L8 images. The analysis was conducted using cloud-free and high-quality images from Area 1 and Area 2 in 2021. Specific dates of L8 and MOD21A2 images employed in Area 1 and Area 2 are presented in Table 2.

Table 2. List of remote sensing data used, including Landsat-8 (L8) and MOD21A2.

Area	Dates of Landsat-8 Images	Dates of MOD21A2
Area 1	10 January 2021, 27 February 2021, 31 March 2021, 2 May 2021, 18 May 2021, 3 June 2021, 19 June 2021, 6 August 2021, 7 September 2021, 10 November 2021, 26 November 2021, 12 December 2021, and 28 December 2021	17 January 2021, 25 January 2021, 2 February 2021, 10 February 2021, 18 February 2021, 14 March 2021, 22 March 2021, 30 March 2021, 7 April 2021, 15 April 2021, 23 April 2021, 1 May 2021, 17 May 2021, 25 May 2021, 2 June 2021, 18 June 2021, 4 July 2021, 21 August 2021, 29 August 2021, 6 September 2021, 14 September 2021, 30 September 2021, 8 October 2021, 16 October 2021, 24 October 2021, 9 November 2021, 17 November 2021, 25 November 2021, 3 December 2021, 11 December 2021, 19 December 2021, and 27 December 2021
Area 2	1 January 2021, 17 January 2021, 2 February 2021, 18 February 2021, 22 March 2021, 7 April 2021, 10 June 2021, 1 November 2021, 17 November 2021, 3 December 2021, and 19 December 2021	1 January 2021, 9 January 2021, 17 January 2021, 25 January 2021, 2 February 2021, 10 February 2021, 18 February 2021, 26 February 2021, 14 March 2021, 22 March 2021, 30 March 2021, 7 April 2021, 15 April 2021, 23 April 2021, 1 May 2021, 9 May 2021, 17 May 2021, 25 May 2021, 2 June 2021, 10 June 2021, 18 June 2021, 26 June 2021, 4 July 2021, 28 July 2021, 5 August 2021, 21 August 2021, 29 August 2021, 6 September 2021, 14 September 2021, 30 September 2021, 8 October 2021, 16 October 2021, 24 October 2021, 1 November 2021, 9 November 2021, 17 November 2021, 25 November 2021, 3 December 2021, 11 December 2021, 19 December 2021, and 27 December 2021

2.2.3. Meteorological Data

Meteorological stations include Daxing Station and Huailai Station, which played a pivotal role in this study. The T_a served as the basis for calculating the LST on a point scale, thereby enabling the comparison of the behavior of the derived time series LST. The Daxing station is located within Daxing District (39.65°N, 116.25°E). This station furnishes data measurements every 30 min, encompassing metrics such as precipitation, wind speed, T_a, air humidity, and sunshine hours. With its extensive record of meteorological elements, the station has significantly contributed to various research endeavors [41–43]. The Huailai station (40.35°N, 115.79°E), located in Donghuayuan Town, Huailai County, features an irrigated corn underlying surface. The meteorological data utilized in this study emanates from the multi-scale surface flux and meteorological elements observation dataset covering the Haihe basin. These datasets were obtained from the National Tibetan Plateau Data Center (http:data.tpdc.ac.cn, accessed on 1 January 2023).

The in situ LST used in this study was converted from the measured T_a, mainly based on the research results of Jiang et al. [44], who believed that there was an obvious linear correlation between T_a and LST. The study mainly used the principles and methods of meteorological statistics and climatology to analyze the daily mean T_a from 1955 to 1999 and the daily LST from 1981 to 1999 of the surface meteorological station in Haidian, Beijing, and established a prediction model of LST based on T_a, which has been widely application [45,46].

2.3. Methods

This section delineates the applied methodologies, encompassing data validation approaches (evaluation indicators), L8 LST retrieval, and the implementation of the ESTARFM. To ensure a comprehensive assessment of outcomes and ascertain the dependability and resilience of the ESTARFM LST, three distinct evaluation metrics were thoughtfully selected. Leveraging an atmospheric correction technique facilitated the retrieval of LST from L8. Subsequently, the ESTARFM was identified as the optimal data fusion method. The research strategies are visually depicted in Figure 2.

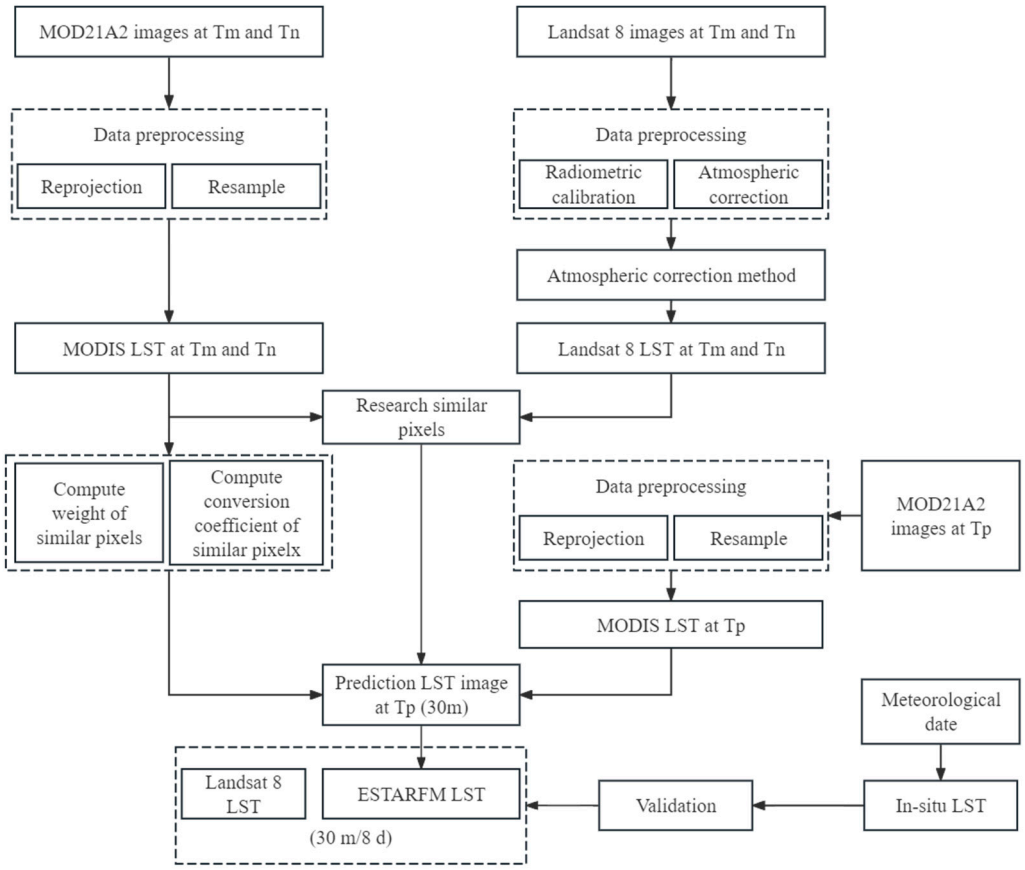


Figure 2. Flowchart of research strategies. T_m and T_n are two pairs of dates that appear simultaneously with MOD21A2 and Landsat 8; T_p is the date when MOD21A2 appears in the middle of T_m and T_n.

2.3.1. Evaluation Metrics

For a comprehensive assessment of the estimated LST, three evaluation metrics were employed: the coefficient of determination (R^2), the mean absolute error (MAE), and the root mean square error (RMSE). In this study, the LST derived through the ESTARFM was employed as the predicted values, while the LST extracted from L8 served as the corresponding measured values on identical days. This approach was adopted to assess the efficacy and versatility of the ESTARFM for LST prediction within the context of the Haihe basin. Additionally, for the validation of time series outcomes, both the ESTARFM LST and L8 LST were considered as estimation values at concurrent moments. Concurrently, the LST computed using T_a was regarded as the measured value, facilitating the validation of time series LST results. The evaluation metrics are calculated as follows [47]:

$$R^2 = \frac{\sum_{i=1}^{n} (P_i - \overline{P})^2}{\sum_{i=1}^{n} (M_i - \overline{P})^2} \quad (1)$$

$$MAE = \frac{1}{n} \sum_{i=1}^{n} |P_i - M_i| \quad (2)$$

$$RMSE = \sqrt{\frac{1}{n} \sum_{i=1}^{n} (P_i - M_i)^2} \quad (3)$$

where n is the number of validation values; M_i and P_i are the measured and predicted LST, respectively; $\overline{P}$ is the average value of the predicted LST.

2.3.2. LST Retrieval Model

The atmospheric correction method functions by gauging the influence of the atmosphere on surface heat radiation and subsequently deducting this influence from the overall heat radiation detected by satellite sensors. This deduction yields the surface radiation intensity, which is further converted into the corresponding LST. The procedural execution is as follows: the thermal infrared radiation brightness value (L_λ) captured by the satellite sensor comprises three components. These include atmospheric upward radiation brightness ($L_\uparrow$), representing the authentic radiation brightness energy that travels through the atmosphere to reach the satellite sensor, and the energy reflected after the atmospheric radiation reaches the ground.

The L_λ can be formulated as follows [48]:

$$L_\lambda = \left[\varepsilon B(T_s) + (1-\varepsilon)L_\downarrow\right]\tau + L_\uparrow \tag{4}$$

where ε is the surface emissivity, which is obtained through the Normalized Differential Vegetation Index (NDVI) threshold method as detailed in the work of Yin et al. [49]; $B(T_s)$ is the brightness of blackbody thermal radiation; $W{\cdot}m^{-2}{\cdot}sr^{-1}{\cdot}\mu m^{-1}$; τ is the atmospheric transmittance in the thermal infrared band; $L_\downarrow$ and $L_\uparrow$ are the atmospheric downward radiation brightness and atmospheric upward radiation brightness, respectively; $W{\cdot}m^{-2}{\cdot}sr^{-1}{\cdot}\mu m^{-1}$. $B(T_s)$ can be obtained according to the radiation transfer equation, and the calculation formula is as follows [48]:

$$B(T_s) = \left[L_\lambda - L_\uparrow - \tau\cdot(1-\varepsilon)L_\downarrow\right]/\tau\cdot\varepsilon \tag{5}$$

where τ, $L_\downarrow$, and $L_\uparrow$ can be automatically obtained by inputting information including the acquisition time of the image, latitude and longitude of the center, and atmospheric pressure in the study area on the NASA (http://atmcorr.gsfc.nasa.gov/, accessed on 1 January 2023).

After estimating $B(T_s)$, LST can be obtained according to the inverse function of Planck's law. The calculation formula is as follows [48]:

$$\mathrm{LST} = K_2/\ln\left(\frac{K_1}{B(T_s)} + 1\right) \tag{6}$$

For TIRS Band 10, K_1 and K_2 are constants (K_1 = 774.89 $W{\cdot}m^{-2}{\cdot}sr^{-1}{\cdot}\mu m^{-1}$; K_2 = 1321.08 K).

2.3.3. ESTARFM

Zhu et al. [29] proposed the ESTARFM, which can effectively complement the advantages of different remote sensing data to generate images with appropriate spatiotemporal resolution. ESTARFM utilizes temporal sequence information to address data gaps and noise to a certain degree. It has the capability to interpolate high-resolution image information from continuous observations of low-resolution imagery, thus reducing issues caused by data gaps or noise. This method was initially applied to the spatial downscaling of low-level remote sensing data, such as surface albedo (α). This method is now applied to high-level remote sensing data of different spatial resolutions, such as L8 LST and MODIS LST, with the purpose of realizing spatial downscaling of remote sensing data of different levels and sources, so as to meet the demand of LST with high spatiotemporal resolution in the study area. The calculation formulas of high spatial resolution images in the prediction period are as follows:

$$L_k(x_{w/2}, y_{w/2}, t_p) = L(x_{w/2}, y_{w/2}, t_k) + \sum_{i=1}^{N} W_i V_i \left(M(x_i, y_i, t_p) - M(x_i, y_i, t_k)\right)(k = m, n) \tag{7}$$

$$L(x_{w/2}, y_{w/2}, t_p) = T_m L_m(x_{w/2}, y_{w/2}, t_p) + T_n L_n(x_{w/2}, y_{w/2}, t_p) \tag{8}$$

$$T_k = \frac{1/\left|\sum_{j=1}^{w}\sum_{i=1}^{w} M(x_i, y_i, t_k) - \sum_{j=1}^{w}\sum_{i=1}^{w} M(x_i, y_i, t_p)\right|}{\sum_{k=m,n}\left(1/\left|\sum_{j=1}^{w}\sum_{i=1}^{w} M(x_i, y_i, t_k) - \sum_{j=1}^{w}\sum_{i=1}^{w} M(x_i, y_i, t_p)\right|\right)}(k = m, n) \quad (9)$$

where w is the search window for similar pixels; $(x_{w/2}, y_{w/2})$ is the position of the central pixel; (x_i, y_i) is the ith similar pixel; $L(x_{w/2}, y_{w/2}, t_k)$ and $M(x_i, y_i, t_k)$ are the LST images of high and low spatial resolution in the k (k = m, n) period; $M(x_i, y_i, t_p)$ are the LST images of low spatial resolution in the p period; $L_m(x_{w/2}, y_{w/2}, t_p)$ and $L_n(x_{w/2}, y_{w/2}, t_p)$ are the LST images with a high spatial resolution of t_p period predicted by high and low spatial resolution images of tm and t_n periods; $L(x_{w/2}, y_{w/2}, t_p)$ is the LST image with high spatial resolution in the prediction period; V_i is the conversion coefficient; T_m and T_n are the temporal weight between the time of tm and t_n, respectively; W_i is the comprehensive weight factor, and its expressions are as follows:

$$W_i = (1/D_i)/\sum_{i=1}^{N}(1/D_i) \quad (10)$$

$$D_i = (1 - R_i)d_i \quad (11)$$

$$d_i = 1 + \sqrt{(x_{w/2} - x_i)^2 + (y_{w/2} - y_i)^2}/(w/2) \quad (12)$$

$$R_i = \frac{E[(L_i - E(L_i))(M_i - E(L_i))]}{\sqrt{D(L_i)} \times \sqrt{D(M_i)}} \quad (13)$$

$$L_i = L(x_i, y_i, t_m, b_1), \cdots, L(x_i, y_i, t_m, b_n), L(x_i, y_i, t_n, b_1), \cdots, L(x_i, y_i, t_n, b_n) \quad (14)$$

$$M_i = M(x_i, y_i, t_m, b_1), \cdots, M(x_i, y_i, t_m, b_n), M(x_i, y_i, t_n, b_1), \cdots, M(x_i, y_i, t_n, b_n) \quad (15)$$

where R_i is the spectral weight; d_i is the spatial distance weight; L_i and M_i are the spectral vector of the *ith* pixel with high and low spatial resolution, respectively; $E(.)$ is the expected value; $D(.)$ is the variance; b_1~b_n are pixel eigenvalues. More details about the ESTARFM procedure can be found in Zhu et al. [29].

3. Results

3.1. Validation of ESTARFM LST and Landsat 8 LST

A rectangular range of 12 km × 12 km was selected in Daxing District (Area 1) and Huailai County (Area 2), respectively, which was mainly referred to in [50]. The selected areas contain a variety of land use types, such as farmland, forest, water, and buildings. Figure 3 shows the comparison between L8 LST and ESTARFM LST in Area 1. The four days without cloud are selected for comparison, which are 2 May, 18 May, 3 June, and 7 September 2021, respectively. Compared with MODIS LST, L8 LST and ESTARFM LST have finer spatial information, which can better reflect spatial differences. On the same day, L8 LST and ESTARFM LST shows similar spatial variation trends, but the variation did not have a strong regularity. For some days, such as 3 June 2021, the L8 LST and ESTARFM LST were significantly different, and the LST of the middle part of the fusion results was significantly higher than that of L8 LST. This is mainly due to the different adjacent dates selected during the fusion process. Due to the influence of the cloud, the fusion result of 3 June 2021 is predicted based on two dates (18 May 2021 and 7 September 2021). However, the time span between 7 September 2021 and 3 June 2021 is long, so there may be some errors. As seen in Figure 3, the LST in the four days ranges from 291 K to 320 K, and the LST in the construction area is significantly higher than that in farmland, forest, and other land use types.

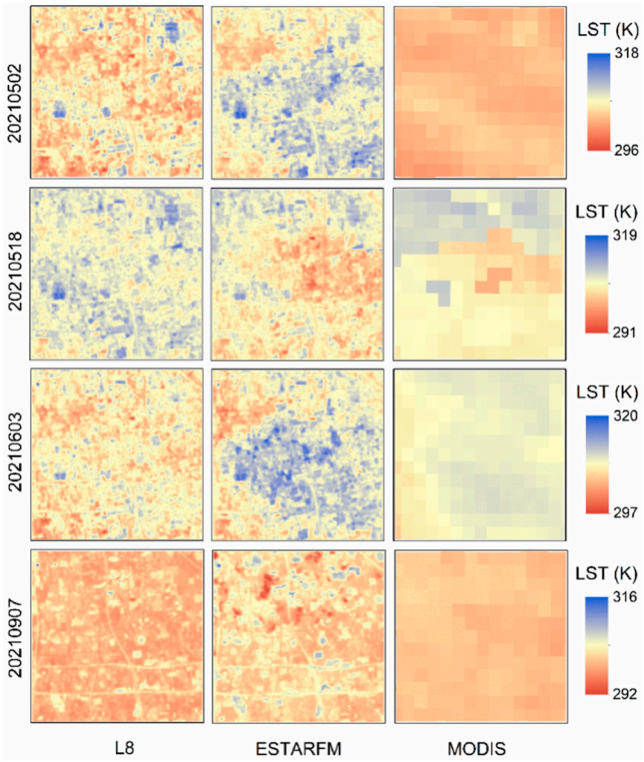


Figure 3. Spatial distributions of L8 LST, ESTARFM LST, and MODIS LST within a sub-study area of 12 km × 12 km in Area 1 on 2 May, 18 May, 3 June, and 7 September 2021, respectively.

Figure 4 shows the scatter diagram of L8 LST and ESTARFM LST on the four days (2 May, 18 May, 3 June, and 7 September 2021). There are 3000 pixels selected for comparison randomly. The ESTARFM LST shows good performance at different dates with a R^2, MAE, and RMSE ranging from 0.41 to 0.84, 0.74 to 1.9 K, and 0.93 to 2.18 K, respectively. At the same time, the fusion results of 18 May 2021 showed the best performance, and the scatter points were distributed on both sides of the 1:1 line. The fusion results of 2 May 2021 were mostly higher than the L8 LST, and the fusion results of 7 September 2021 were relatively poor (R^2 = 0.41, MAE = 1.90 K, and RMSE = 2.18 K). These results are different from those of other studies in the Haihe River basin. Abowarda et al. [40] conducted a downscaling on soil moisture in the Haihe River basin. Since LST is an important downscaling factor, data fusion was also carried out on LST. The downscaled LST achieved R, bias, MAE, and RMSE of 0.94 (0.90), 0.707 K (1.122 K), 1.013 K (1.133 K), and 1.134 K (1.184 K) on 18 April 2016 (10 September 2016). Long et al. [34] also carried out a two-date LST downscaling study in the Hehai basin with the bias, MAE, RMSE, and R of the downscaled LST images during the winter wheat (summer maize) period, which were −1.53 K (−0.00 K), 1.64 K (0.72 K), 1.86 K (0.91 K), and 0.93 (0.89), respectively. It can be seen the accuracy of some dates obtained in this study is better than that obtained in other studies, while the accuracy of individual dates is lower. But overall, the results of this study are satisfactory.

Figure 5 shows the spatial distributions of L8 LST, ESTARFM LST, and MODIS LST within a sub-study area of 12 km × 12 km in Area 2 on 17 January, 2 February, 18 February, and 22 March 2021, respectively. Compared with MODIS LST, L8 LST and ESTARFM LST have finer spatial information, which can better reflect spatial differences. On the same day, the spatial variation trends of L8 LST and ESTARFM LST were similar, and the spatial difference characteristics were more obvious than those of Area 1. In the upper right of Area 2, there is a reservoir named Guanting Reservoir. Regardless of whether it is MODIS LST, L8 LST, or ESTARFM LST, the spatial location of the reservoir can be clearly seen. The LST of the reservoir is lower than that of other regions, which accords with our common

sense. In the seasons of the four days, the LST was generally low, with the lowest reaching 262 K. In March, due to the gradual increase in T_a, the LST gradually increased, with the maximum reaching 300 K.

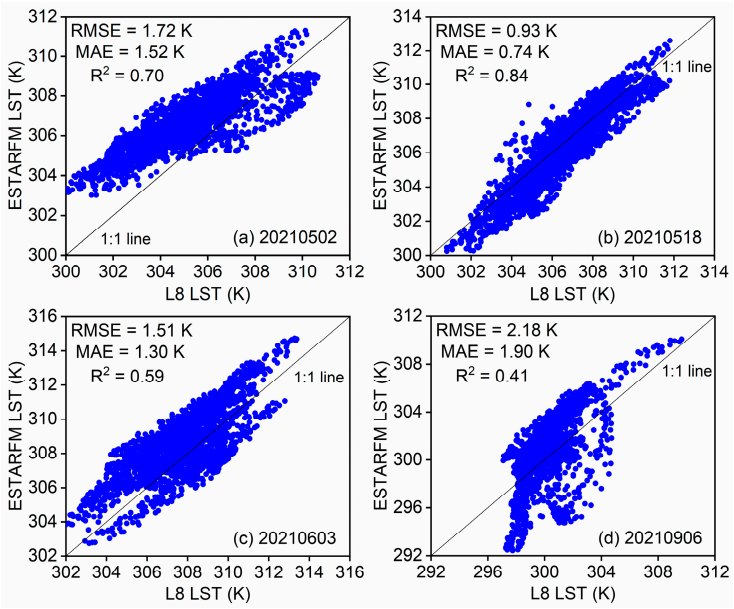


Figure 4. Validation of ESTARFM LST versus L8 LST for the four days, i.e., 2 May 2021 (**a**), 18 May 2021 (**b**), 3 June 2021 (**c**), and 6 September 2021 (**d**).

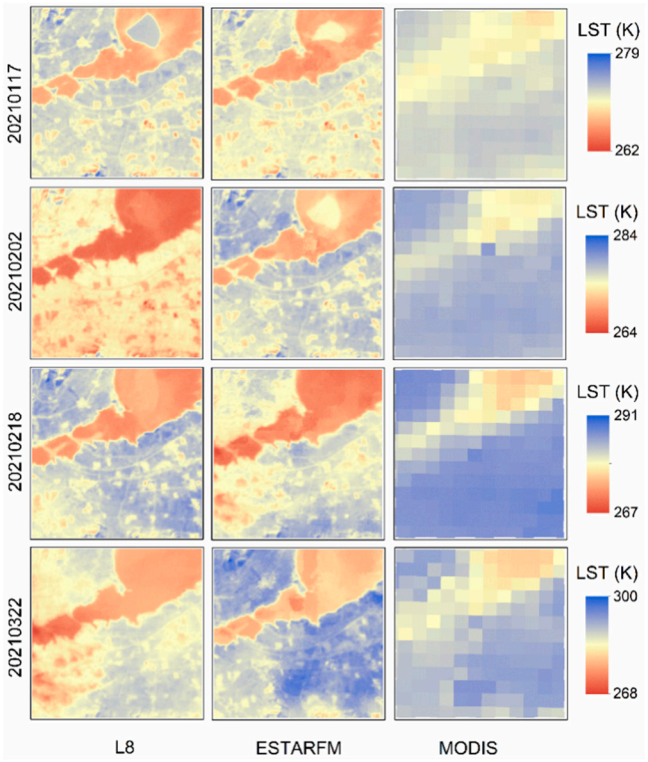


Figure 5. Spatial distributions of L8 LST, ESTARFM LST, and MODIS LST within a sub-study area of 12 km × 12 km in Area 2 on 17 January, 2 February, 18 February, and 22 March 2021, respectively.

Figure 6 shows the scatter diagram of L8 LST and ESTARFM LST on the four days (17 January, 2 February, 18 February, and 22 March 2021). There are 3000 pixels selected for comparison randomly. The ESTARFM LST shows good performance at different dates

with a R^2, MAE, and RMSE ranging from 0.89 to 0.97, 0.70 to 2.43 K, and 0.83 to 2.63 K, respectively. As seen in Figure 6, the fusion results of 2 February 2021 have the best performance, and the scatter points are distributed on both sides of the 1:1 line. The fusion results of 17 January 2021 and 18 February 2021 are mostly lower than that of L8 LST.

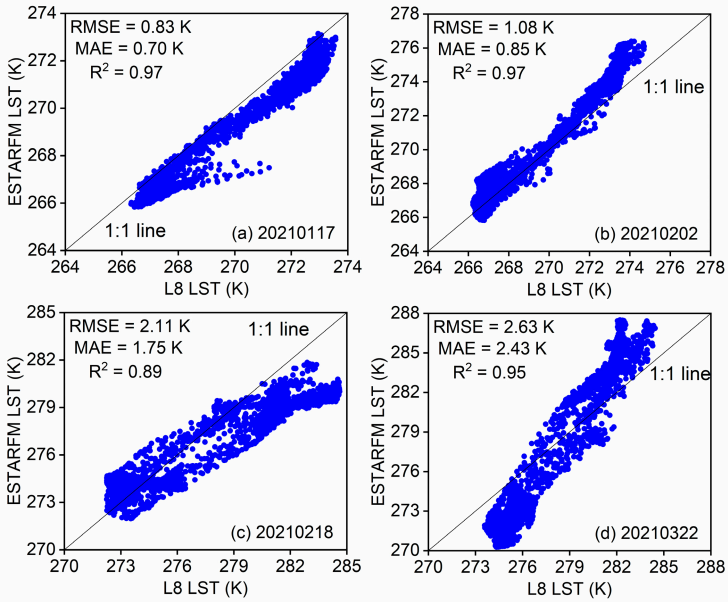


Figure 6. Validation of ESTARFM LST versus L8 LST for the four days, i.e., 17 January 2021 (**a**), 2 February 2021 (**b**), 18 February 2021 (**c**), and 22 March 2021 (**d**). LST = land surface temperature.

3.2. Validation of ESTARFM LST and the In Situ LST

Since this study used T_a for indirect validation in the study area, the feasibility of calculating LST by T_a should first be validated. Data from a long-term observation station in Lixin County, Bozhou, Anhui province, were selected, and the monitoring time was from 1 October 2020 to 15 April 2022. At the same time, the T_a and LST calculation formula ($LST = 1.1588T_a - 1.1416$) [44] were used to obtain the calculated LST, which was compared with the LST measured by instruments to obtain the scatter plot (Figure 7). As can be seen from Figure 7, R^2, RMSE, and MAE are 0.933, 3.108 K, and 2.243 K, respectively. The validation result is good; therefore, it can be considered this formula is feasible, and this also proves it is feasible to use T_a to calculate LST indirectly to validate LST obtained by L8 inversion and data fusion.

In order to further evaluate the applicability and robustness of the fusion method in the Haihe basin, the changes in fusion LST and L8 LST and the in situ LST at Daxing station and Huailai station were studied (Figure 8). The period of high LST occurs in June, July, and August, reaching 300 K for most of the time, while the period of low LST is about 260–270 K in January and December. The change trends of the in situ LST and fusion LST and L8 LST at the two stations are basically similar, showing the characteristics of first increasing and then decreasing. The precipitation characteristics of the two stations were different. The precipitation in Area 1 mainly occurred from July to September, and the maximum was 42.42 mm on 20 August 2021. The precipitation in Area 2 mainly occurred from May to September, and the maximum was 38.3 mm on 17 July 2021. The influence of precipitation on the LST of the two stations was different. In Area 1, from January to July, the fusion LST and L8 LST were higher than the in situ LST by about 5 K. After precipitation in August, the in situ LST was gradually consistent with the fusion LST and L8 LST, with a R^2 of 0.72, a MAE of 10.85 K, and a RMSE of 12.48 K, respectively (Figure 9).

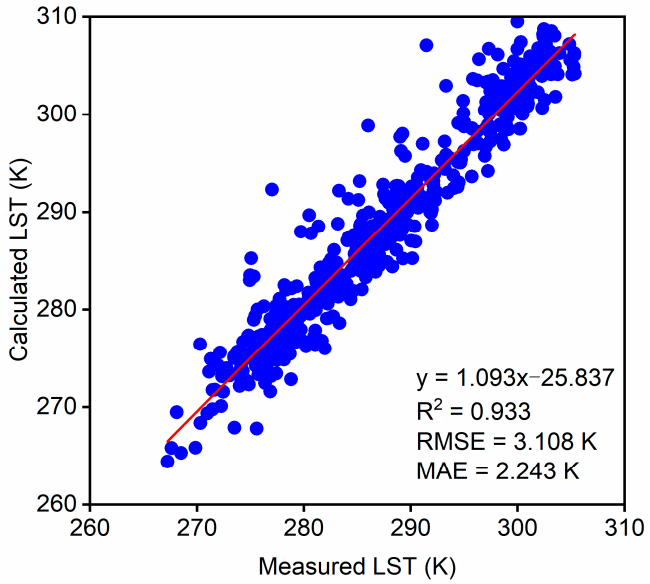


Figure 7. Feasibility validation of using T_a to calculate land surface temperature (LST).

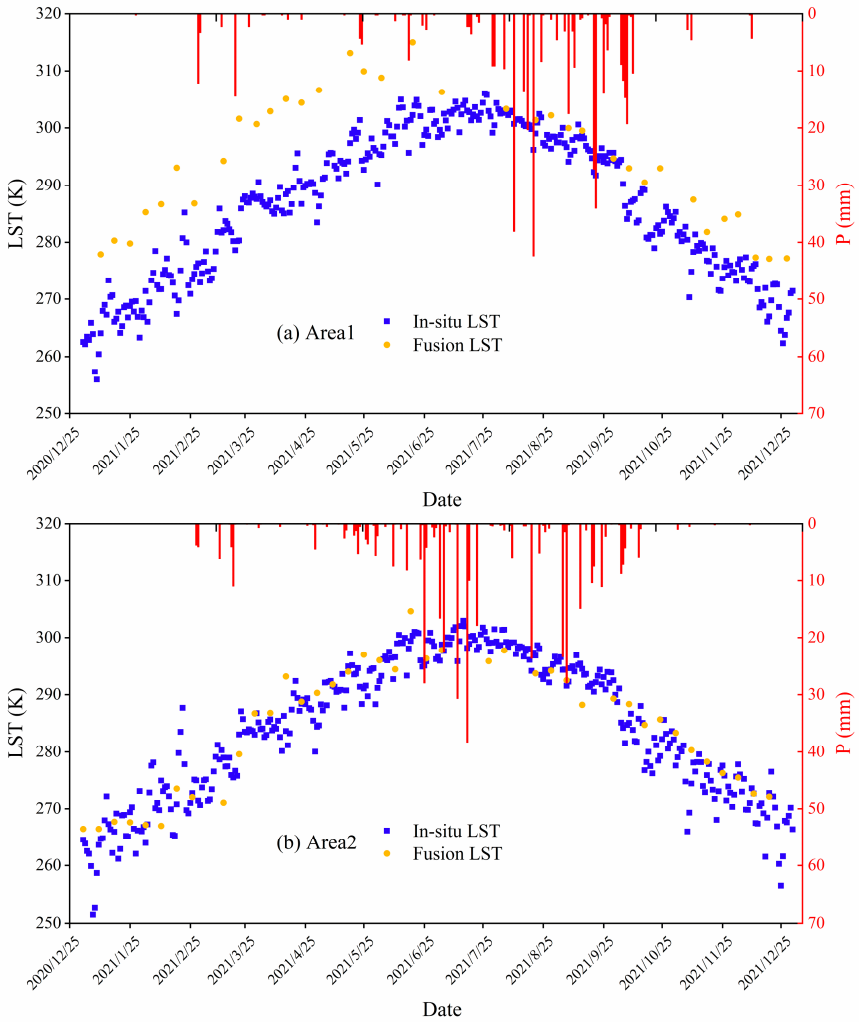


Figure 8. Comparison of the in situ LST and fusion LST and L8 LST at Daxing station and Huailai station. (**a**) Area 1; (**b**) Area 2. LST = land surface temperature.

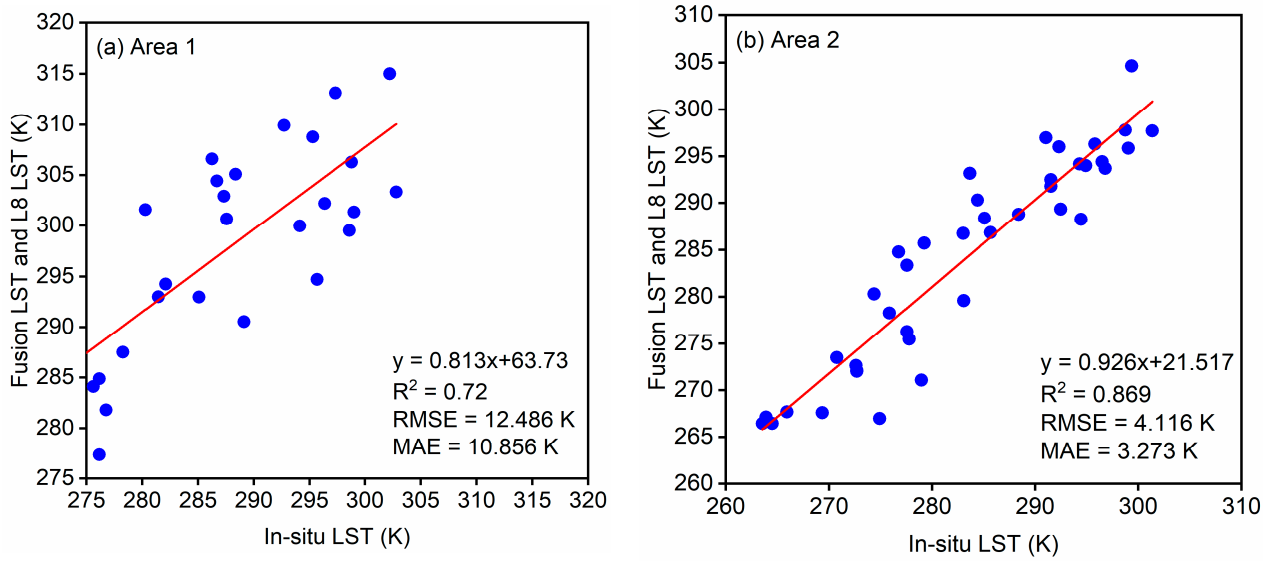


Figure 9. Scatter plot of the in situ LST and fusion LST and L8 LST at Daxing station and Huailai station. (**a**) Area 1; (**b**) Area 2. LST = land surface temperature.

3.3. Analysis of the Time and Spatial Variation within the Year

The L8 LST and ESTARFM LST were used to obtain the monthly LST in Daxing District and Huailai County (Figures 10 and 11). As seen in Figure 10, from January to December, LST presented a feature of first increasing and then decreasing, and a turning point was reached in August, with a gradual increase from January to August and a gradual decrease from September to December. LST was abnormal in July, and the LST in the west of Daxing District was low, which was not in line with common sense. This is mainly due to the poor quality of L8 data due to the rainy weather in July, which makes it impossible to obtain enough effective data for LST fusion. In 2021, the lowest and highest LST of Daxing District are 254 K and 326 K, respectively. As seen in Figure 11, LST in Huailai showed a feature of first increasing and then decreasing in 2021. July was the turning point. LST gradually increased from January to June, reached the maximum in July, and gradually decreased from August to December. Compared with Area 1, the turning point of Area 2 occurred in July rather than August, which may be related to the different geographical locations of the two areas, the larger building area of Area 1 and the longer duration of high LST. The LST characteristics of Guanting Reservoir in Huailai County are very obvious, and the water surface temperature is lower than other land use types. In December, January, February, and March, when the water surface temperature of the reservoir is lower than 273.15 K, the water surface will freeze. In 2021, the lowest LST in Huailai County is 255 K and the highest is 315 K. Compared with Daxing District, LST is lower in most areas of Huailai County, which is closely related to land use types in the two study areas. Daxing District is located in the suburb of Beijing, China. It has a large building coverage and lacks large rivers. Therefore, under the same climate conditions, LST is relatively high. There is a large reservoir in Huailai County, i.e., Guanting Reservoir, and the forest coverage area is large, and the larger the forest coverage, the lower the LST.

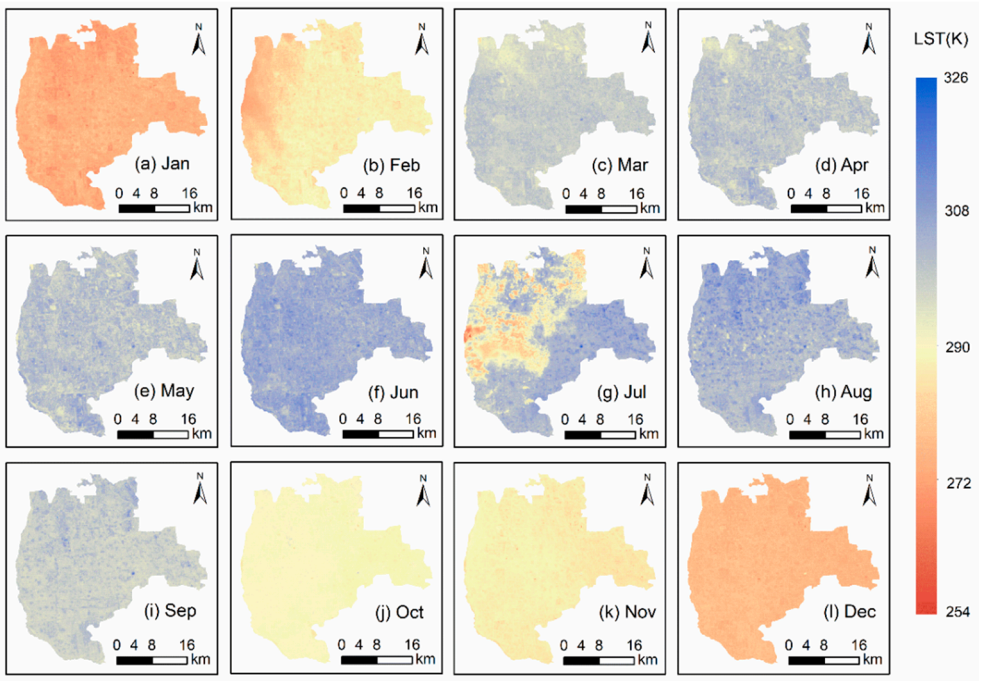


Figure 10. Spatial distribution of monthly LST in Daxing District in 2021. LST = land surface temperature.

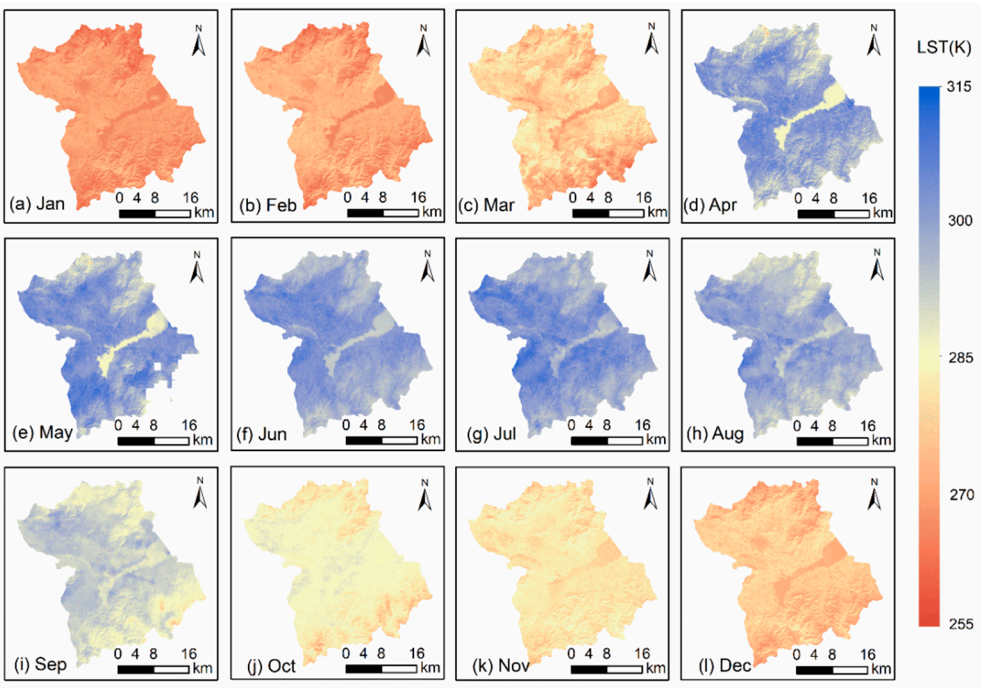


Figure 11. Spatial distribution of monthly LST in Huailai County in 2021. LST = land surface temperature.

4. Discussion

4.1. Error Sources

The correlation between the L8 LST and ESTARFM LST on 6 September 2021 was notably poor. This phenomenon can be attributed to significant rainfall on 5 September 2021, leading to the accumulation of water in certain regions. The persistence of these water-covered areas on September 6 resulted in a substantial water surface extent. This stark contrast in land cover types between the wet conditions and the T_m and T_n periods introduced significant discrepancies. As a result, when employing data fusion algorithms, considerable errors were encountered due to these differences in surface conditions. The

fusion results of different dates are inconsistent, which is mainly caused by the different adjacent dates selected in the fusion process, and the date selection is completely determined by the data quality. In general, the ESTARFM performs well in the application of obtaining LST with a spatiotemporal resolution of 8 d and 30 m in the Haihe basin. It provides data support for the study of urban thermal environment, resource utilization, and land planning, and also provides important model input parameters for soil moisture downscaling. In Area 2, the in situ LST and ESTARFM LST were not affected by precipitation, and the coincidence between the ESTARFM LST and in situ LST was perfect (R^2 = 0.87, MAE = 2.27 K, and RMSE = 4.12 K), which was better than that in Area 1. This may be caused by different types of land use. There are many buildings around farmland in Area 1, and the building surface temperature is greatly affected by precipitation. The farmland in Area 2 is basically contiguous, and there is a large reservoir near the station. However, the sensitivity of water surface temperature and farmland surface temperature to precipitation is low.

In the process of data fusion using the ESTARFM, two adjacent times are not fixed, but two adjacent times need to be chosen according to the quality of MOD21A2 and L8. The closer the two adjacent moments are to the prediction moment, the higher the prediction accuracy is. In the process of data fusion in this study, the interval of two adjacent dates at each prediction moment is different, which may bring some errors. Meanwhile, there are many other data fusion algorithms, such as the FSDAF [30] and the CESTEM [31]. The performance of these methods in the fusion of LST was not compared in this study. Yang et al. [51] fused the FSDAF method to generate high spatiotemporal resolution LST, and the R^2 between the fused images and AWS LST products was greater than or equal to 0.64, which was better than the result obtained in this study ($R^2 \geq 0.41$). The reason for this difference may be caused by the climate inconsistency in the two study areas.

In terms of the validation method, this study uses L8 LST as the benchmark data to validate the LST obtained by this method, which is consistent with the practice [35]. Abowarda et al. [35] conducted a study on soil moisture downscaling in the Haihe basin. First, the NDVI, LST, and α, which are important surface parameters, need to be downscaled in space, and then the downscaling results are compared with the L8 calculation or retrieving results.

In terms of time series LST validation, this study uses meteorological data to calculate LST, so as to validate the stability and robustness of time series LST. It is easy to obtain meteorological data, which is a convenient source of validation data in areas lacking in situ LST. However, there may be errors in the T_a model for calculating LST, and the applicability of the model may change under different climate types and different underlying surface types, which we did not study. At the same time, we found that many studies used measured LST as validation data when carrying out research on LST. Yang et al. [52] validated the LST with a high spatial resolution generated by the ESTAREM in the Heihe basin with the in situ LST. The results show that the R^2 between the predicted LST and the in situ LST is higher than 0.71, the MAE is lower than 2.00 K, and the RMSE is lower than 2.60 K, which has a good prediction accuracy.

4.2. Prospects

We tested the method in Daxing District and Huailai County to demonstrate the applicability and robustness of the ESTARFM in the application of LST fusion in the Haihe basin and obtained LST products with a spatiotemporal resolution of 8 d and 30 m. This study can provide data support for urban thermal environment, resource utilization, and land planning, and also provide a key downscaling factor for soil moisture downscaling. But there are still challenges.

It is difficult to solve the problem of data source quality. Terra, Aqua, and L8 are all optical satellites. Their signal transmission is affected by clouds and rain, and it is not possible to ensure that the satellite can obtain remote sensing data at all transit times with good quality. Many scholars have developed a series of cloud removal algorithms [53]

or spatial interpolation methods [54] to solve the problem of data quality, but the data obtained by these methods is not real. To substantially improve the problem, it may also need to start with the satellite sensors themselves. In the future, we hope to develop sensors that have a wide range and are not affected by clouds and rain. At the same time, Amazirh et al. [32] introduced the Sentinel-1 data to downscale MOD11A1 to a spatial resolution of 100 m. The approaches are tested over two heterogonous sites: an 8 km × 8 km irrigated perimeter and a 12 km × 12 km rainfed area south of Marrakech during the growing season in 2015–2016.

Our study can only obtain LST with a temporal resolution of 8 d, but if the LST can be obtained with a continuous time, it will greatly promote the application of LST. Daily surface temperature products, such as MOD21A1, have serious data missing and low spatial resolution, so they cannot be applied in actual production. In future studies, CLDAS LST can be introduced on the basis of this method, and LST products with a spatiotemporal resolution of 1 d and 30 m can be obtained by using a data fusion algorithm. At the same time, our study has been tested in the subregion of the Haihe basin, which can be expanded in the future to obtain LST products at a regional scale.

5. Conclusions

In this study, the fusion of multi-source remote sensing data to generate high spatial resolution LST was tested in the Haihe basin. Using multi-temporal MOD21A2 and L8 images, LST with the same temporal resolution as MOD21A2 and the same spatial resolution as L8 is estimated based on the ESTARFM. Based on the validation of the ESTARFM LST and L8 LST, as well as the ESTARFM LST and in situ LST, the following conclusions can be summarized:

(1) The ESTARFM is applicable to the heterogeneous area of the Haihe basin and can obtain LST images with a high spatial resolution, which have clear texture and depict spatial details.
(2) The comparison between ESTARFM LST and L8 LST shows the R^2 of most days was higher than 0.59, the MAE was lower than 2.43 K, and the RMSE was lower than 2.63 K, showing a good fusion effect.
(3) The comparison between ESTARFM LST and in situ LST shows a high validation accuracy, with a R^2, MAE, and RMSE of 0.87, 2.27 K, and 4.12 K, respectively. The produced time series LST has the characteristics of good quality, high reliability, and strong robustness.
(4) During the year, the LST in the study area shows a trend of first increasing and then decreasing, and the maximum appeared in July or August. The LST in the construction area was higher than that in farmland, forest, water, and other land use types.

Author Contributions: Methodology, R.L.; Data processing, H.C.; Formal analysis, M.J.; Funding acquisition, Z.W.; Project administration, B.Z.; Validation, C.H. All authors have read and agreed to the published version of the manuscript.

Funding: This research was funded by the National Key Research and Development Program of China (No. 2022YFD1900500), the National Key Research and Development Program of China (No. 2023YFD1900801-02), the Chinese National Science Fund (52130906), and the Independent Research Project of State Key Laboratory of Simulation and Regulation of Water Cycle in River Basin (SKL2022TS13).

Data Availability Statement: The data presented in this study are available upon request from the first author (R.L.).

Acknowledgments: We thank the editors and the reviewers for their outstanding comments and suggestions, which greatly helped us improve the technical quality of the manuscript.

Conflicts of Interest: The authors declare no conflicts of interest.

References

1. Wu, P.; Yin, Z.; Zeng, C.; Duan, S.-B.; Gottsche, F.-M.; Ma, X.; Li, X.; Yang, H.; Shen, H. Spatially Continuous and High-Resolution Land Surface Temperature Product Generation: A review of reconstruction and spatiotemporal fusion techniques. *IEEE Geosci. Remote Sens. Mag.* **2021**, *9*, 112–137. [CrossRef]
2. Quan, J.; Guan, Y.; Zhan, W.; Ma, T.; Wang, D.; Guo, Z. Generating 60–100 m, hourly, all-weather land surface temperatures based on the Landsat, ECOSTRESS, and reanalysis temperature combination (LERC). *ISPRS J. Photogramm. Remote Sens.* **2023**, *205*, 115–134. [CrossRef]
3. Li, Z.-L.; Wu, H.; Duan, S.-B.; Zhao, W.; Ren, H.; Liu, X.; Leng, P.; Tang, R.; Ye, X.; Zhu, J.; et al. Satellite Remote Sensing of Global Land Surface Temperature: Definition, Methods, Products, and Applications. *Rev. Geophys.* **2023**, *61*, e2022RG000777. [CrossRef]
4. Meng, Q.; Zhang, L.; Sun, Z.; Meng, F.; Wang, L.; Sun, Y. Characterizing spatial and temporal trends of surface urban heat island effect in an urban main built-up area: A 12-year case study in Beijing, China. *Remote Sens. Environ.* **2018**, *204*, 826–837. [CrossRef]
5. Qiao, Z.; Liu, L.; Qin, Y.; Xu, X.; Wang, B.; Liu, Z. The Impact of Urban Renewal on Land Surface Temperature Changes: A Case Study in the Main City of Guangzhou, China. *Remote Sens.* **2020**, *12*, 794. [CrossRef]
6. Yang, C.; Yan, F.; Lei, X.; Ding, X.; Zheng, Y.; Liu, L.; Zhang, S. Investigating Seasonal Effects of Dominant Driving Factors on Urban Land Surface Temperature in a Snow-Climate City in China. *Remote Sens.* **2020**, *12*, 3006. [CrossRef]
7. Amazirh, A.; Er-Raki, S.; Chehbouni, A.; Rivalland, V.; Diarra, A.; Khabba, S.; Ezzahar, J.; Merlin, O. Modified Penman–Monteith equation for monitoring evapotranspiration of wheat crop: Relationship between the surface resistance and remotely sensed stress index. *Biosyst. Eng.* **2017**, *164*, 68–84. [CrossRef]
8. Olivera-Guerra, L.; Merlin, O.; Er-Raki, S.; Khabba, S.; JoseEscorihuela, M. Estimating the water budget components of irrigated crops: Combining the FAO-56 dual crop coefficient with surface temperature and vegetation index data. *Agric. Water Manag.* **2018**, *208*, 120–1331. [CrossRef]
9. Song, L.; Liu, S.; Kustas, W.P.; Nieto, H.; Sun, L.; Xu, Z.; Skaggs, T.H.; Yang, Y.; Ma, M.; Xu, T.; et al. Monitoring and validating spatially and temporally continuous daily evaporation and transpiration at river basin scale. *Remote Sens. Environ.* **2018**, *219*, 72–88. [CrossRef]
10. Amazirh, A.; Merlin, O.; Er-Raki, S.; Gao, Q.; Rivalland, V.; Malbeteau, Y.; Khabba, S.; Escorihuela, M.J. Retrieving surface soil moisture at high spatio-temporal resolution from a synergy between Sentinel-1 radar and Landsat thermal data: A study case over bare soil. *Remote Sens. Environ.* **2018**, *211*, 321–337. [CrossRef]
11. Tagesson, T.; Horion, S.; Nieto, H.; Fornies, V.Z.; González, G.M.; Bulgin, C.E.; Ghent, D.; Fensholt, R. Disaggregation of SMOS soil moisture over West Africa using the Temperature and Vegetation Dryness Index based on SEVIRI land surface parameters. *Remote Sens. Environ.* **2018**, *206*, 424–441. [CrossRef]
12. Zhao, Z.; Wang, H.; Qin, D.; Wang, C. Large-scale monitoring of soil moisture using Temperature Vegetation Quantitative Index (TVQI) and exponential filtering: A case study in Beijing. *Agric. Water Manag.* **2021**, *252*, 106896. [CrossRef]
13. Long, D.; Yan, L.; Bai, L.; Zhang, C.; Li, X.; Lei, H.; Yang, H.; Tian, F.; Zeng, C.; Meng, X.; et al. Generation of MODIS-like land surface temperatures under all-weather conditions based on a data fusion approach. *Remote Sens. Environ.* **2020**, *246*, 111863. [CrossRef]
14. Sheffield, J.; Wood, E.; Pan, M.; Beck, H.; Coccia, G.; Serrat-Capdevila, A.; Verbist, K. Satellite Remote Sensing for Water Resources Management: Potential for Supporting Sustainable Development in Data-Poor Regions. *Water Resour. Res.* **2018**, *54*, 9724–9758. [CrossRef]
15. Ford, T.W.; Quiring, S.M. Comparison of Contemporary In Situ, Model, and Satellite Remote Sensing Soil Moisture with a Focus on Drought Monitoring. *Water Resour. Res.* **2019**, *55*, 1565–1582. [CrossRef]
16. Qin, Z.; Karnieli, A.; Berliner, P. A Mono-Window Algorithm for Retrieving Land Surface Temperature from Landsat TM data and its Application to the Israel-Egypt Border Region. *Int. J. Remote Sens.* **2010**, *22*, 3719–3746. [CrossRef]
17. Yu, Y.; Tarpley, D.; Privette, J.L.; Goldberg, M.D.; Raja, M.K.R.V.; Vinnikov, K.Y.; Xu, H. Developing Algorithm for Operational GOES-R Land Surface Temperature Product. *IEEE Trans. Geosci. Remote Sens.* **2009**, *47*, 936–951. [CrossRef]
18. Sobrino, J.A.; Li, Z.L.; Stoll, M.P.; Becker, F. Multi-channel and multi-angle algorithms for estimating sea and land surface temperature with ATSR data. *Int. J. Remote Sens.* **2007**, *17*, 2089–2114. [CrossRef]
19. Shi, C.; Xie, Z.; Qian, H.; Liang, M.; Yang, X. China land soil moisture EnKF data assimilation based on satellite remote sensing data. *Sci. China Earth Sci.* **2011**, *54*, 1430–1440. [CrossRef]
20. Xia, Y.; Ek, M.; Wei, H.; Meng, J. Comparative analysis of relationships between NLDAS-2 forcings and model outputs. *Hydrol. Processes* **2012**, *26*, 467–474. [CrossRef]
21. Rodell, M.; Houser, P.R.; Jambor, U.; Gottschalck, J.; Mitchell, K.; Meng, C.-J.; Arsenault, K.; Cosgrove, B.; Radakovich, J.; Bosilovich, M.; et al. The Global Land Data Assimilation System. *Bull. Am. Meteorol. Soc.* **2004**, *85*, 381–394. [CrossRef]
22. Li, X.; Zhou, Y.; Asrar, G.R.; Zhu, Z. Creating a seamless 1 km resolution daily land surface temperature dataset for urban and surrounding areas in the conterminous United States. *Remote Sens. Environ.* **2018**, *206*, 84–97. [CrossRef]
23. Xu, S.; Cheng, J. A new land surface temperature fusion strategy based on cumulative distribution function matching and multiresolution Kalman filtering. *Remote Sens. Environ.* **2021**, *254*, 112256. [CrossRef]
24. Yu, W.; Nan, Z.; Wang, Z.; Chen, H.; Wu, T.; Zhao, L. An Effective Interpolation Method for MODIS Land Surface Temperature on the Qinghai–Tibet Plateau. *IEEE J. Sel. Top. Appl. Earth Obs. Remote Sens.* **2015**, *8*, 4539–4550. [CrossRef]

25. Januar, T.W.; Lin, T.-H.; Huang, C.-Y.; Chang, K.-E. Modifying an Image Fusion Approach for High Spatiotemporal LST Retrieval in Surface Dryness and Evapotranspiration Estimations. *Remote Sens.* **2020**, *12*, 498. [CrossRef]
26. Li, W.; Huang, J.; Yang, L.; Chen, Y.; Fang, Y.; Jin, H.; Sun, H.; Huang, R. A Practical Remote Sensing Monitoring Framework for Late Frost Damage in Wine Grapes Using Multi-Source Satellite Data. *Remote Sens.* **2021**, *13*, 3231. [CrossRef]
27. Zhang, X.; Zhou, J.; Liang, S.; Wang, D. A practical reanalysis data and thermal infrared remote sensing data merging (RTM) method for reconstruction of a 1-km all-weather land surface temperature. *Remote Sens. Environ.* **2021**, *260*, 112437. [CrossRef]
28. Gao, F.; Masek, J.; Schwaller, M.; Hall, F.G. On the Blending of the Landsat and MODIS Surface Reflectance: Predicting Daily Landsat Surface Reflectance. *IEEE Trans. Geosci. Remote Sens.* **2006**, *44*, 2207–2218. [CrossRef]
29. Zhu, X.; Chen, J.; Gao, F.; Chen, X.; Masek, J.G. An enhanced spatial and temporal adaptive reflectance fusion model for complex heterogeneous regions. *Remote Sens. Environ.* **2010**, *114*, 2610–2623. [CrossRef]
30. Zhu, X.; Helmer, E.H.; Gao, F.; Liu, D.; Chen, J.; Lefsky, M.A. A flexible spatiotemporal method for fusing satellite images with different resolutions. *Remote Sens. Environ.* **2016**, *172*, 165–177. [CrossRef]
31. Houborg, R.; McCabe, M.F. A Cubesat enabled Spatio-Temporal Enhancement Method (CESTEM) utilizing Planet, Landsat and MODIS data. *Remote Sens. Environ.* **2018**, *209*, 211–226. [CrossRef]
32. Amazirh, A.; Merlin, O.; Er-Raki, S. Including Sentinel-1 radar data to improve the disaggregation of MODIS land surface temperature data. *ISPRS J. Photogramm. Remote Sens.* **2019**, *150*, 11–26. [CrossRef]
33. Kou, X.; Jiang, L.; Bo, Y.; Yan, S.; Chai, L. Estimation of Land Surface Temperature through Blending MODIS and AMSR-E Data with the Bayesian Maximum Entropy Method. *Remote Sens.* **2016**, *8*, 105. [CrossRef]
34. Long, D.; Bai, L.; Yan, L.; Zhang, C.; Yang, W.; Lei, H.; Quan, J.; Meng, X.; Shi, C. Generation of spatially complete and daily continuous surface soil moisture of high spatial resolution. *Remote Sens. Environ.* **2019**, *233*, 111364. [CrossRef]
35. Abowarda, A.S.; Bai, L.; Zhang, C.; Long, D.; Li, X.; Huang, Q.; Sun, Z. Generating surface soil moisture at 30 m spatial resolution using both data fusion and machine learning toward better water resources management at the field scale. *Remote Sens. Environ.* **2021**, *255*, 112301. [CrossRef]
36. Xu, S.; Cheng, J.; Zhang, Q. A Random Forest-Based Data Fusion Method for Obtaining All-Weather Land Surface Temperature with High Spatial Resolution. *Remote Sens.* **2021**, *13*, 2211. [CrossRef]
37. Weng, Q.; Fu, P.; Gao, F. Generating daily land surface temperature at Landsat resolution by fusing Landsat and MODIS data. *Remote Sens. Environ.* **2014**, *145*, 55–67. [CrossRef]
38. Han, Y.; Jia, D.; Zhuo, L.; Sauvage, S.; Sánchez-Pérez, J.-M.; Huang, H.; Wang, C. Assessing the Water Footprint of Wheat and Maize in Haihe River Basin, Northern China (1956–2015). *Water* **2018**, *10*, 867. [CrossRef]
39. Knauer, K.; Gessner, U.; Fensholt, R.; Kuenzer, C. An ESTARFM Fusion Framework for the Generation of Large-Scale Time Series in Cloud-Prone and Heterogeneous Landscapes. *Remote. Sens.* **2016**, *8*, 425. [CrossRef]
40. Dong, S. Problems and Solutions of Rural Water Supply in Beijing Daxing District. *Tianjin Agric. Sci.* **2019**, *25*, 82–86. [CrossRef]
41. Zhao, N.; Liu, Y.; Cai, J.; Paredes, P.; Rosa, R.D.; S.Pereira, L. Dual crop coefficient modelling applied to the winter wheat–summer maize crop sequence in North China Plain: Basal crop coefficients and soil evaporation component. *Agric. Water Manag.* **2012**, *117*, 93–105. [CrossRef]
42. Han, X.; Wei, Z.; Zhang, B.; Li, Y.; Du, T.; Chen, H. Crop evapotranspiration prediction by considering dynamic change of crop coefficient and the precipitation effect in back-propagation neural network model. *J. Hydrol.* **2021**, *596*, 126104. [CrossRef]
43. Han, X.; Zhou, Q.; Zhang, B.; Che, Z.; Weib, Z.; Qiu, R.; Chen, H.; Li, Y.; Du, T. Real-time methods for short and medium-term evapotranspiration forecasting using dynamic crop coefficient and historical threshold. *J. Hydrol. Hydromech.* **2022**, *606*, 127414. [CrossRef]
44. Jiang, H.; Liao, S.; Erike, A. Statistical Analysis on Relationship Between Soil Surface Temperature and Air Temperature. *Agric. Meteorol.* **2004**, *25*, 1–4. [CrossRef]
45. Wang, E.L.; Zhang, A.Q.; Bao, T.E.; Liu, X.C. Variability analysis of freezing depth mode of vertical buried pipes with different materials in cold area. *J. Hydraul. Eng.* **2016**, *48*, 86–95. [CrossRef]
46. Wang, N.; Lv, Z.; Xu, J.; Zhang, H.; Zhang, X. Difference of temperature distribution characteristics based on remote sensing and meteorological station temperature data. *Natl. Remote Sens. Bull.* **2021**, *25*, 1848–1861. [CrossRef]
47. Lin, R.; Chen, H.; Wei, Z.; Li, Y.; Zhang, B.; Sun, H.; Cheng, M. Improved Surface Soil Moisture Estimation Model in Semi-Arid Regions Using the Vegetation Red-Edge Band Sensitive to Plant Growth. *Atmosphere* **2022**, *13*, 930. [CrossRef]
48. Ma, S.; Pu, Z. Research on Surface Temperature Inversion Algorithm Based on Landsat8 Data in Urumqi City. *Comput. Digit. Eng.* **2020**, *48*, 2316–2320. [CrossRef]
49. Yin, C.L.; Meng, F.; Yu, Q.R. Calculation of land surface emissivity and retrieval of land surface temperature based on a spectral mixing model. *Infrared Phys. Technol.* **2020**, *108*, 103333. [CrossRef]
50. Bai, L.; Long, D.; Yan, L. Estimation of Surface Soil Moisture with Downscaled Land Surface Temperatures Using a Data Fusion Approach for Heterogeneous Agricultural Land. *Water Resour. Res.* **2019**, *55*, 1105–1128. [CrossRef]
51. Yang, M.; Yang, G.J.; Chen, X.N.; Zhang, Y.F.; You, J.N. Generation of land surface temperature with high spatial and temporal resolution based on FSDAF method. *Remote Sens. Nat. Resour.* **2018**, *30*, 54–62. [CrossRef]
52. Yang, G.; Sun, C.; Li, H. Verification of high-resolution land surface temperature by blending ASTER and MODIS data in Heihe River Basin. *Trans. Chin. Soc. Agric. Eng.* **2015**, *31*, 193–200.

53. Zeng, C.; Long, D.; Shen, H.; Wu, P.; Cui, Y.; Hong, Y. A two-step framework for reconstructing remotely sensed land surface temperatures contaminated by cloud. *ISPRS J. Photogramm. Remote Sens.* **2018**, *141*, 30–45. [CrossRef]
54. Kilibarda, M.; Hengl, T.; Heuvelink, G.B.M.; Gräler, B.; Pebesma, E.; Tadić, M.P.; Bajat, B. Spatio-temporal interpolation of daily temperatures for global land areas at 1 km resolution. *J. Geophys. Res. Atmos.* **2014**, *119*, 2294–2313. [CrossRef]

Disclaimer/Publisher's Note: The statements, opinions and data contained in all publications are solely those of the individual author(s) and contributor(s) and not of MDPI and/or the editor(s). MDPI and/or the editor(s) disclaim responsibility for any injury to people or property resulting from any ideas, methods, instructions or products referred to in the content.